A Mesoscale Study of Pinch-off under High Strain

M. Arienti[1*], X. Li[2]
[1]Sandia National Laboratories, Livermore, 94550 CA, USA
[2]United Technologies Research Center, East Hartford, 06108 CT, USA
marient@sandia.gov and lixy2@utrc.utc.com

Abstract

We study the dynamic behavior of a pinching liquid thread as a function of the time to pinch-off. The novelty of this work resides in the use of a particle method (the Many-body Dissipative Particle Dynamics method, or MDPD), and in the inclusion of the interaction with a surrounding gas. As an MDPD calculation can be carried out at a scale below the continuity limit as a coarse-grained molecular simulation, this work represent a mesoscale approach to the study of spray formation.

Two issues are discussed in this paper. First, adding the effect of a second MDPD fluid requires the characterization of the friction interaction between particles of two immiscible fluids: unlike interfacial tension or solubility, this parameter does not have a directly related physical property. Second, in order to subject the liquid thread to a straining field, a two-phase, Non-Periodic Boundary Condition (NPBC) needs to be implemented. In the proposed NPBC method, two layers of particles are built into the domain on each side of the computational box. The outermost layer is modified at every iteration by placing particles of the prescribed type: this buffer works as a barrier whose composition depends on the instantaneous location of the boundary. The innermost layer contains thermalized particles that are otherwise free to move according to the distribution of the surrounding particles.

By enabling the simulation of pinch-off under extensional flow, an arbitrary strain rate can be imposed via the gas phase. The capillary number Ca therefore appears as an additional parameter controlling pinch-off, and the simulations illustrate the role of stochastic effects for a range of Ca values.

Introduction

The objective of this study is the dynamic behavior of a pinching liquid thread of minimum radius h_{min} as a function of the time to breakup, t_0-t, in the presence of shear from the gas phase. In free-surface flows, the advantage of methods like Dissipative Particle Dynamics (DPD) resides in the simplicity of the underlying algorithm of particle interaction under a soft repulsive potential. Substantially less expensive than Molecular Dynamics (MD), DPD can be formally constructed from coarse-graining of Lennard-Jones clusters [1]. The occurrence of capillary pinch-off has been demonstrated by a modified DPD method [2], as well as by pioneering MD simulations [3]. This latter work explored the domain, up to a few hundreds of nanometers, where thermal fluctuations at the liquid interface become relevant.

Surface tension emerges from the asymmetry of the intermolecular forces acting on a layer of molecules at the liquid-vapor interface. As this asymmetry causes larger intermolecular distances in the outer layer than in the liquid bulk, the forces in that layer act to contract the interface. In the Many-body DPD (MDPD) method by Pagonabarraga and Frenkel [4], the amplitude of the soft repulsion is made proportional to the local density of the particles, thus achieving a cubic pressure-density relation. A longer-range attractive force is also active. MDPD has been extensively investigated by Warren [5] and Trofimov et al. [6]. The dependence of surface tension coefficient, σ, on the interaction parameters is discussed by Arienti et al. [7].

As it will be shown later, single-component MDPD simulations can capture the complete sequence of scaling behaviors – inviscid, inertial-viscous and stochastically-dominated – that emerge in the asymptotic analysis of slender jets when the effect of the gas phase is negligible. To calculate pinch-off under an extensional field, a novel, two-phase, Non-Periodic Boundary Condition (NPBC) algorithm is introduced to impose a specific velocity profile and phase composition along the domain boundaries. After highlighting the MDPD method, we focus on the determination of the inter-particle coefficient for liquid-gas interaction. No general approach is found for this problem, but a set of interaction coefficients is determined for typical liquid-gas density and viscosity ratios. The power law behavior of the minimum radius of a capillary thread is reviewed before briefly discussing simulations of pinch-off in an extensional flow.

Simulations are enabled by the particle dynamics software code LAMMPS (Large-scale Atomic/Molecular Massively Parallel Simulator) [8], to which a new MDPD class was added. The computationally scalable imple-

* Corresponding author: marient@sandia.gov

mentation of LAMMPS, which guarantees the optimization of the particle interaction calculation through an efficient neighbor list algorithm, will not be discussed here.

Numerical method

MDPD inherits the three pairwise-additive inter-particle forces formulation of the standard DPD scheme. The conservative, dissipative and random forces are defined, respectively, as

$$\mathbf{F}_{ij}^{C} = F_{ij}^{C}(r_{ij})\hat{\mathbf{r}}_{ij} \tag{1}$$

$$\mathbf{F}_{ij}^{D} = -\gamma\ \omega_D(r_{ij})\ (\mathbf{v}_{ij}\cdot\hat{\mathbf{r}}_{ij})\hat{\mathbf{r}}_{ij} \tag{2}$$

$$\mathbf{F}_{ij}^{R} = \vartheta_{ij}\xi\ \omega_R(r_{ij})\ \hat{\mathbf{r}}_{ij} \tag{3}$$

where $\hat{\mathbf{r}}_{ij} = \mathbf{r}_{ij}/r_{ij}$ and $\mathbf{v}_{ij} = \mathbf{v}_i - \mathbf{v}_j$ for a pair of particles *i* and *j*.

The repulsive force depends on a weighted average of the local density, whereas the attractive force is density-independent, following the approach by Warren [5]:

$$\mathbf{F}_{ij}^{C} = A_{ij}\omega_c(r_{ij}) + B_{ij}(\bar{\rho}_i + \bar{\rho}_j)\omega_d(r_{ij}). \tag{4}$$

The weight functions $\omega_c(r) = (1 - r/r_c)$ and $\omega_d(r) = (1 - r/r_d)$ vanish for $r > r_c$ and $r > r_d$, respectively. Since a DPD method with a single range may not have a stable interface [9], in Equation (4) the repulsive contribution is set to act at a shorter range $r_d < r_c$ than the soft pair attractive potential. The many-body repulsion is derived from a self-energy per particle which is quadratic in the local density, $B_{ij}(\bar{\rho}_i + \bar{\rho}_j)\omega_d(r_{ij})$, where $B > 0$. The MDPD number density is defined as

$$\bar{\rho}_i = \sum_{j\neq i}\omega_\rho(r_{ij}) \tag{5}$$

and its weight function ω_ρ is

$$\omega_\rho(r) = \frac{15}{2\pi r_d^3}(1 - r/r_d)^2. \tag{6}$$

This kernel vanishes for $r > r_d$ and is normalized for convenience: $\int d^3\mathbf{r}\omega_\rho(r) = 1$.

The MDPD thermostat is the same as the DPD thermostat. It consists of random and dissipative forces, which maintain the equilibrium temperature *T* through the condition posed by the fluctuation-dissipation theorem

$$\xi^2 = 2\gamma k_B T, \tag{8}$$

with $\left(\omega_{ij}^{R}\right)^2 = \omega_{ij}^{D}$. k_B is the Boltzmann constant. $\mathbf{F}_{ij}^{R}$ is modeled as a Gaussian distribution with zero first moment and second moment proportional to the temperature. The θ_{ij} coefficients from Eq. 3 are independent identically distributed Gaussian random numbers with zero mean and unit variance. Thus, the dissipative force $\mathbf{F}_{ij}^{D}$ acts to reduce the kinetic energy of the particle and is compensated by the random motion induced by the stochastic part, $\mathbf{F}_{ij}^{R}$. The weight function for the dissipative force is

$$\omega_D(r) = (1 - r/r_c)^2 \quad . \tag{9}$$

Details about the choice of the random and friction coefficients, ξ and γ, can be found in [9].

Since the random and dissipative forces in MDPD and DPD are of the same nature, particles from the two schemes can be easily combined. This enables the simulation of more complex flows, for instance the inclusion of a surrounding gas. Table 1 offers an example of two different sets of parameters: the first two rows correspond to MDPD fluids (the same parameter combination was considered by Groot and Warren [9]), the third to a DPD gas.

The simulations presented in this work are all carried out with the velocity Verlet algorithm by Groot and Warren [9] with parameter value 1/2. In the DPD gas, the sign of the coefficient *A* is switched and there is no density-dependent term ($B = 0$). The values on the left of the dividing line in Table 1 are the input interaction coefficients, while the values on the right are the corresponding properties of the fluid. Lacking an attractive force component, the surface tension coefficient is not an intrinsic property of the DPD gas and does not appear on the table. The last column reports the number density *n*. From these parameters, we verify that the density ratio between fluid (1) and (3) is $\rho_3/\rho_1 = (m_3 n_3)/(n_1 m_1) = 0.0013$, and that the kinematic viscosity ratio is $\nu_3/\nu_1 = 15$. These two values are in the range of typical air/liquid ratios for air at ambient conditions.

m	A	r_c	B	r_d	γ	ξ	ν	σ	n
1	-40	1	25	0.75	0.5	1	0.84	7.3	6.1
1	-40	1	40	0.75	72	12	3.6	4.7	5.1
0.0064	10	1	0	0	288	24	13	--	1.2

Table 1. Example of parameter sets for DPD and MDPD fluids: from top to bottom, liquid 1, liquid 2, and gas.

Viscosity at a gas-liquid interface

As noted in the previous section, the viscosity of a DPD fluid is controlled by γ and the corresponding random force coefficient ξ. In a two-component system, where each fluid has its own friction factor, γ_{11} and γ_{22}, the problem is to define the interaction between particles of unlike fluids, γ_{12}. This factor lacks a related physical property, such as interfacial tension or solubility, to specify its value. In fact, a study [10] carried out with two distinct DPD fluids – and with the addition of specular reflection to keep them separated at the interface – reported that γ_{12} can affect the velocity profile even away from the interface.

The periodic Poiseuille flow (PPF) is commonly used to evaluate the viscosity of a DPD fluid [11]. The method is reviewed here for the general case of two immiscible fluids with distinct properties. The fluids are forced in opposite direction along the z axis by body forces, while periodic boundary conditions are applied on all sides. This setup generates two opposite parabolic profiles of velocity. Taking the opposing particle forces to be applied to two adjacent volumes of common depth D, height H and width, W_1 and W_2, the force magnitudes must equilibrate so that $f_1N_1 + f_2N_2 = 0$, where N_1 and N_2 are the total numbers of particles on the two sides.

At steady state, the Navier-Stokes equations reduce to

$$\mu \frac{d^2 w}{dx^2} = \frac{N_i f_i}{W_i HD} \tag{10}$$

in the transverse coordinate x (w is the z-component of velocity). The body force can be thought of as a pressure uniformly distributed on a surface of size W_iD for a length H. The integration of the equation above yields

$$w = \frac{1}{\mu_i} \frac{N_i f_i W_i}{2HD} \left(\zeta^2 - \zeta \right) + w_s, \tag{11}$$

where $\zeta = x/H$. The surface velocity, w_s, is identically zero in the case of a single-component PPF flow with two equal half-volumes. In the general case, this value can be calculated by assuming that, on average, all particles start from rest in the simulation. The mass flow rates through the two half-volumes must then remain on average equal and opposite,

$$\int_{W_1} m_1 n_1 w_1 dx + \int_{W_2} m_2 n_2 w_2 dx = 0. \tag{12}$$

This leads to

$$w_s = -\frac{n_1 W_1 \overline{w_1} + n_2 W_2 \overline{w_2}}{n_1 W_1 + n_2 W_2} = \frac{N_1 \overline{w_1} + N_2 \overline{w_2}}{N_1 + N_2}, \tag{13}$$

where $\overline{w_i}$ is the average of w_i (with sign) in the two half-volumes, and n_i is the number density of the two components, $N_i = W_i n_i HD$. If $W_1 = W_2$, it can be easily verified for a single component that $f_1 = -f_2$, and therefore that w_s is identically zero. This is the configuration typically used to evaluate the kinematic viscosity of the fluid, ν, which is then obtained by integrating the mass flow rate of the time-averaged velocity profile [11],

$$\nu = \frac{W^2 f}{12\, m \overline{w}}. \tag{14}$$

In the two following examples, the calculated velocity profile of a two-component PPF is compared to the solution in equations (11) and (13). Figure 1 is a plot for the two MDPD fluids whose properties are listed in the first two rows of Table 1 (liquid 1 and 2, respectively). The reference solution is composed by two symmetric arcs of parabola joined at $x = W_1 = W_2 = 15$ (in DPD units) with $w_s = -0.046$. Simulations are carried out with

2187 particles of liquid 1 and 2106 particles of liquid 2 – the difference accounting for a slightly larger number density of liquid 1. A 30×5×5 domain and a time step of 0.005 are used.

The inter-particle forces are also modelled as MDPD with the same r_c and r_d. To avoid mixing, B_{12} = 65, larger than both B_{11} and B_{22}, while A_{12} = -40. Increasing B_{12} further causes the two fluids to separate, leaving a non-physical layer where the number density is smaller than in both bulk volumes. Two values of inter-particle friction coefficient are considered: the harmonic mean between γ_{11} and γ_{22}, γ_{12} = 0.496 (square symbols); and the arithmetic mean, γ_{12} = 36.2 (triangles). These two options, both in principle valid, are examined in detail in [10], with the harmonic mean providing the best match with the analytic velocity profile. Contrary to the computational set-up reported there, no specular reflection at the interface is implemented for our calculations. We find that the two velocity profiles in Figure 1 are not substantially different, and that the harmonic mean is slightly closer to the analytic curve.

The second test (Figure 2) is more challenging in that we use both MDPD and DPD fluids, whose properties induce the large difference in density and viscosity that was calculated in the previous Section. The interaction coefficients are listed in the first and third row of Table 1. Also, A_{12} = -5 and B_{12} = 50. Again, the two fluids remain separated at the interface without additional intervention. Simulations are carried out in the same 30×5×5 domain using 2187 particles of liquid 1 and 400 particles of "gas". In relation with these properties, the two analytic velocity profiles, joined at w_s = -0.022, display a very different concavity, with large values of velocity on the gas side (as expected from the much smaller dynamic viscosity). Three values of inter-particle friction coefficient are considered in the plot of Figure 2: γ_{12} = 288, 72, 0.5. The time step is 0.0001 to accommodate the smaller mass of the DPD fluid. None of the resulting velocity profiles from the plot perfectly matches the solution: in fact, as γ_{12} decreases, increasing velocities are obtained in the gas. However, at γ_{12} = 0.5, a value close to the harmonic mean of the friction coefficients, a "velocity slip" in w can be detected at the interface. Conversely, the velocity profile calculated for γ_{12} = 288 is the closest to the analytic profile. Thus, while no generalization can be drawn from this case, the inter-particle parameters A_{12} = -5, B_{12} = 50, and γ_{12} = 288 will be used for the dumbbell simulations.

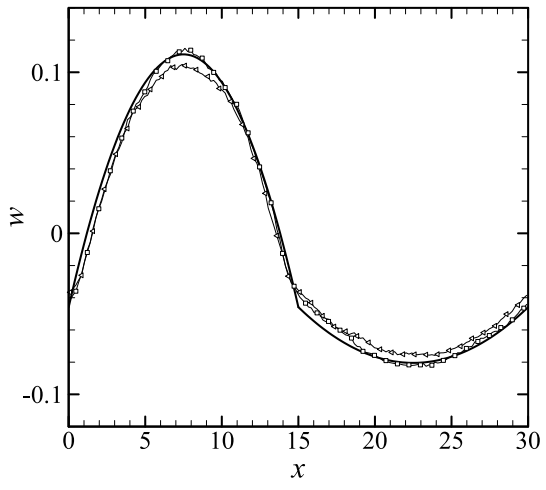

Figure 1. Liquid-liquid PPF. Line: analytic solution; Triangles: inter-particle friction coefficient is calculated from arithmetic mean; Squares: harmonic mean.

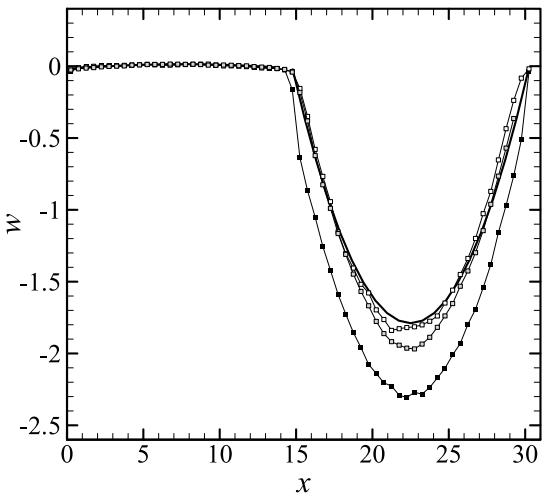

Figure 2. Liquid-gas PPF. Line: analytic solution; Black symbols: γ_{12} = 0.5; Gray symbols: γ_{12} = 72; White symbols: γ_{12} = 288.

Non-Periodic Boundary Conditions

A novel element in this study is the implementation of a Non-Periodic Boundary Condition (NPBC) to broaden the application of particle methods and study straining gas-liquid fields. A first challenge is that the boundary conditions need to include the right amount of attractive force, responsible for the continuity of the liquid. Implementation of a simple reflecting wall alone is not sufficient because there would not be any force anchoring the MDPD boundary particles. Also, an effective-force approach where potential is applied to impose the desired kinematics is insufficient to keep the liquid and gas phase separated.

As shown in the schematics of Figure 3, two layers of particles are built into the domain on each side of the computational box where the NPBC is assigned. The outermost layer (O) is modified at every iteration by placing particles of the prescribed type. This layer is a fixed (no time integration) barrier whose composition depends on the instantaneous location of the boundary interface. Layer (O) provides the necessary attractive force for the continuity of the MDPD liquid.

Particles from the innermost (I) layer of the buffer are free to move according to the distribution of the surrounding particles. At the end of every iteration their velocity is modified so that 1) the average particle velocity of a cell of the buffer matches the prescribed velocity of that buffer; 2) the squared deviation from that average value matches the prescribed temperature. Here, "cell" refers to an element of volume of side $L_i = n_i^{-1/3}$, where n is the number density of component i; see Figure 3. Particles are free to cross in both directions the boundary between the (I) layer and the domain proper, but particles crossing the separation between layers (I) and (O) are reflected back. This wall moves at the velocity of the normal component of $\mathbf{v}_b$.

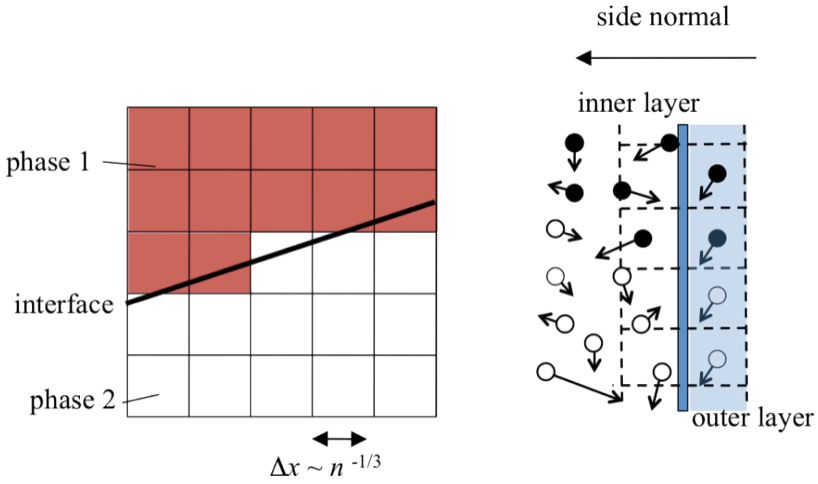

Figure 3. Schematics showing the prescription of composition and velocity at a face boundary.

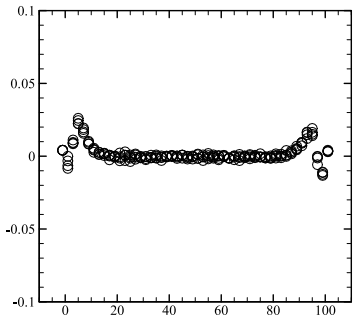

Figure 4. Fraction variation of density profiles at NPBC "walls".

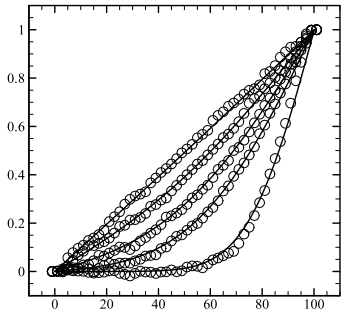

Figure 5. Velocity profiles from impulsively started wall.

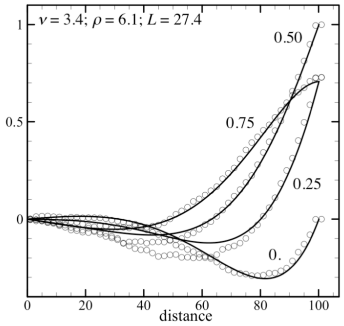

Figure 6. Velocity profiles from periodically oscillating wall.

A simple verification test can be carried out by examining density variations near an impenetrable, standing, boundary. Density oscillations typically affect the near-wall boundary layer because of the difficulty in reproducing the constrained particle dynamic behavior there. A test carried out in a 100^3 box for liquid 1, with the two remaining boundary pairs treated as periodic, shows that there are indeed number density variations with respect to the nominal value, but that such oscillations are limited to less than 3%; see Figure 4.

A second test looks at the shear behavior of a one-component fluid. The right-hand side of the computational domain is impulsively given an upward velocity parallel to the wall. The first and the last symbols of the velocity profile correspond to the imposed velocity at the two outer layers. The calculated profiles can be compared with the unsteady Couette analytical solution [12], shown in Figure 5 as a continuous line. Agreement is good, both in the transient and in the steady state.

The third case study examines the situation where the right-hand side wall is oscillated periodically with angular frequency ω. In that configuration, the flow profile has a maximum amplitude at the moving wall and the transverse linear momentum induced by the motion of the boundary penetrates into a fluid layer of width proportional to $\sqrt{\nu/\omega}$. Beyond this layer the velocity amplitude tends to zero as it approaches the other wall held at rest; see Figure 6. The analytical solution (continuous lines in the plot) is the sum of a periodic term and a transitory one and can be found in Ref. [12]. The computed solution follows the velocity profiles rather well, with the worst match at ¼ of the oscillating cycle.

Results and Discussion

We first review the results for capillary pinch-off in the absence of the gas phase. A number of authors have carried out local analyses of the Navier–Stokes equations for pinching liquid threads; see, for instance, Ref. [13]. For sufficiently small values of the Ohnesorge number, $\mathrm{Oh} = \rho^{1/2}\nu / (R\sigma)^{1/2}$, pinch-off proceeds according to the power law $h_{min} \sim (t_0-t)^{2/3}$. Viscous effects become important as the minimum radius of the thread continues to decrease, until the flow transitions to the inertial-viscous regime where $h_{min} \sim t_0-t$. At even smaller scales, stochastic behavior begins to emerge in the MDPD simulation and h_{min} starts following a power law with exponent 0.418 [14]. The 0.418 power law is predicted from the Stochastic Lubrication Equation (SLE), derived by Moseler and Landman [3] by augmenting the stress tensor with a stochastic Gaussian term: at this stage, any increase of the thread radius also increases its effective mass, slowing down the motion of the fluid, whereas any fluctuation towards a smaller neck radius accelerates pinch-off.

According to these results, it should be possible to observe first the 2/3 slope, then the slope 1, and finally the 0.418 slope in a logarithmic plot of h_{min} vs. time to pinch-off. However, spanning the three scaling behaviors in one simulation has so far proven computationally prohibitive using traditional computational method. This is because the first transition from inviscid behavior depends on Oh, but the second occurs for $h_{min} \sim \mathrm{Oh}^2$, at sub-micron scales for most liquids. In the following example we take a reference jet radius, as well as given fixed values of surface tension and density, and decrease the viscosity of the fluid until all the three regimes appear.

To track the minimum jet radius as a function of time, snapshots of particle positions are post-processed according to the following procedure. The computational domain is first axially divided into 50 bins; then the center of mass of each slice of the jet is calculated. This is a crucial step in measuring the radius profile because the liquid thread can oscillate during the pinch-off process. For each bin, an histogram of number density is constructed in annular rings with a radial increment of 10^{-3} units. The surface of the liquid slice is identified at a position such that 1% or less of the particles of the bin lie outside the surface. This small number of particles is assumed to belong to the vapor phase. The pinch-off time is established as the instant when one of the bins becomes empty. The time to pinch-off τ is normalized by the capillary time scale $(\rho R^3/\sigma)^{1/2}$, whereas h_{min} is normalized by the nominal radius of the thread, R.

The simulation of Figure 7 is carried out with the properties of liquid 1 and an initial perturbation wavelength of 40, using periodic boundaries. The log-log plot of $h_{min}(\tau)$ is shown in Figure 7a for the kinematic viscosity $\nu = 2.8$ (Oh=1.2): stochastic behavior dominates in this case, as indicated by the fact that most of the tracked points are aligned along the slope 0.418. In Figure 7b ($\nu = 0.93$, Oh=0.41), the unit slope, associated with the inertial-viscous regime, begins to appear roughly above $h_{min}/R \sim 0.1$. At a smaller viscosity, $\nu = 0.072$, the 2/3 power inviscid scaling also appears, albeit briefly (Figure 7c). The transition from inviscid to viscous-inertial takes place at $h_{min}/R \sim 0.5$. A snapshot of the simulation immediately after pinch-off is shown in Figure 7d. Additional details can be found in [15]. The comparison with asymptotic analysis results verifies the correctness of the adopted MDPD methodology

We next enforce the extensional configuration displayed in Figure 8a: in an axis-symmetric coordinates, the axial velocity is $v_z = a\,z$, where a is the strain rate, and the radial component is $v_r = -a\,r/2$. The capillary number is $\mathrm{Ca} = \rho\,\nu a\,R/\sigma$, where R is the initial minimum radius of the dumbbell, $R = 6.5$. The flow field is achieved by imposing NPBCs on the sides of a 50^3 box. The time-averaged velocity of the particles arranges itself quickly to a fully developed extensional field. A snapshot of the central slice of the domain is shown in Figure 8b soon after the begin of the simulation.

The domain initially contains 14,512 particles of liquid 1 and 15,924 particles of gas; as time progresses, liquid particles exit the domain while more gas particles enter it. To account for the advection component involved in imposing a prescribed strain rate, the time step is reduced to 0.00004. Thus, a calculation including the interaction with the gas phase is substantially more expensive than the single-component simulations of capillary pinch-off discussed earlier. Also, NPBCs require two additional layers of particles for each boundary pair – a 12% increase in the overall system size.

Three strain rate values are considered in the plot of Figure 9 in units of the inverse of a DPD time: they are $a = 0.2$ (white circles); $a = 0.4$ (grey circles); and $a = 0.8$ (black circles). These values correspond to Ca = 0.91, 1.8, and 3.6 respectively. With increasing strain, the dumbbell becomes a thin thread that tends to fracture in multiple points. The time to pinch-off is actually almost the same for the three cases and comparable to the case without strain. Similar is also the early behavior of h_{min} along the inertial-viscous regime of slope 1. However, a dependence on the capillary number can be observed in the later dynamics of the thread, as the two curves at higher Ca display a faster decrease rate than the 0.418 slope. The amount of scattering in the data points just before pinch-off requires further investigation to determine whether a different power law for h_{min} can emerge at sufficiently large Ca.

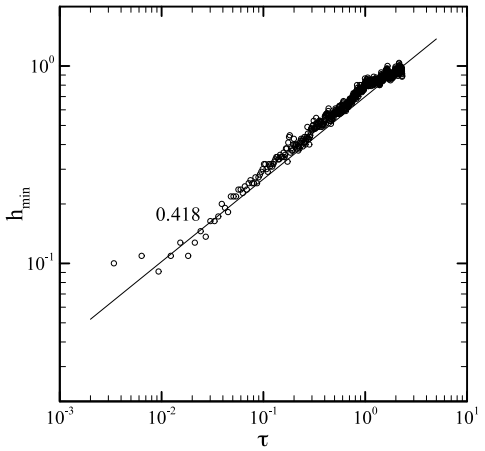

(a) Oh = 1.2 (ν = 2.8)

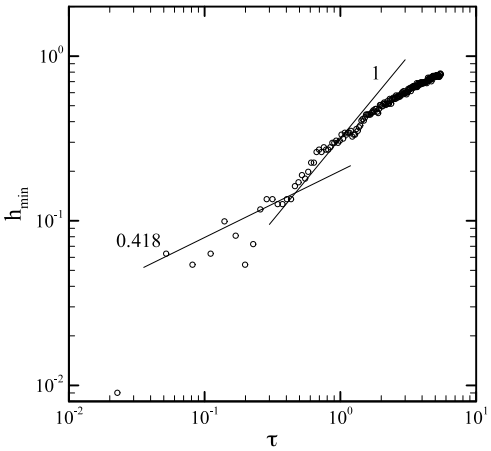

(b) Oh = 0.41 (ν = 0.93)

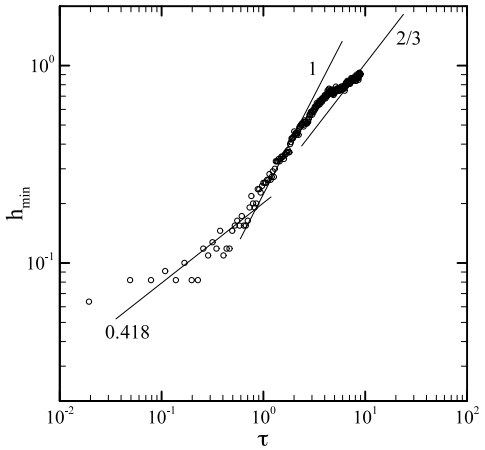

(c) Oh = 0.022 (ν = 0.072)

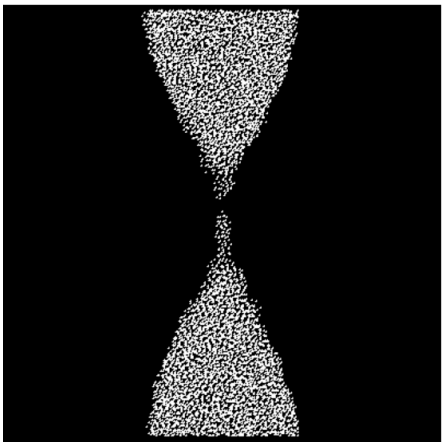

(d) Snapshot after pinch-off

Figure 7. Variation of the minimum liquid thread radius versus the time to pinch-off.

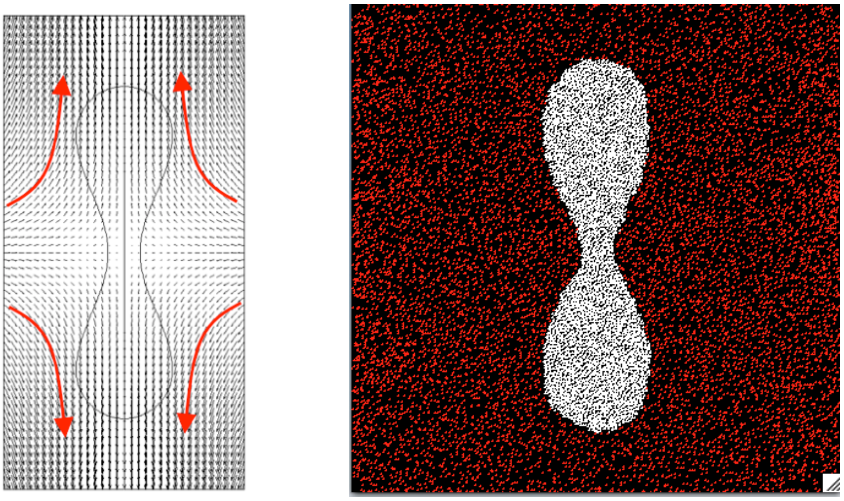

Figure 8. Axis-symmetric dumbbell subject to extensional flow: setup (left) and snapshot of a slice through the domain (right).

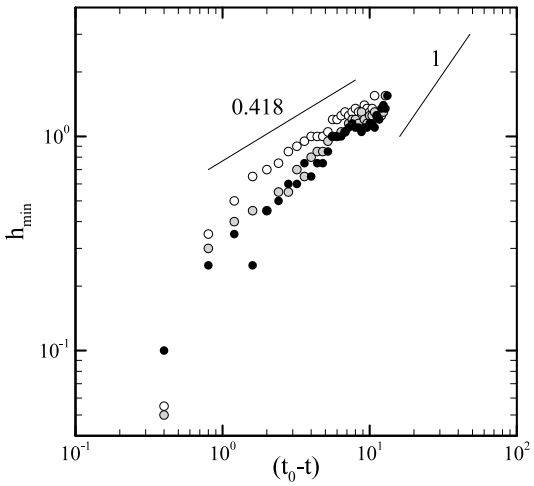

Figure 9. Variation of the minimum liquid thread radius versus the time to pinch-off. White circles: strain rate a = 0.2; gray: a = 0.4; black: a = 0.8.

Summary and Conclusions

The spatial and temporal mesoscales (in the range of 10 to 1000 nm and 1 ns to 10 ms) that can be captured by particle coarse-graining can significantly extend the reach of MD simulations while keeping the fundamental viewpoint that fluid properties arise from elementary particle interactions.

Building on previous work on the asymptotic scaling of capillary pinch-off, we have began to explore shear-driven pinch-off in the limit where the liquid thread surface begins to be affected by thermal fluctuations. Using multiple MDPD fluids requires the assignment of inter-particle coefficients – an area where fundamental studies are lacking. It also requires the capability to impose arbitrary boundary values of velocity and phase: the Non-Periodic Boundary Condition method described in this paper is demonstrated in this context (and could also be used to couple the MDPD simulation with an external continuous discretizations of the two-phase flow). Preliminary results show a dependence of the late stages of pinch-off dynamics on the capillary number, but data are at the moment insufficient to quantify this trend when stochastic behavior emerges.

Acknowledgements

This work was supported by the AFOSR contract AFD-070820-034 under the supervision of Dr. Fariba Fahroo. One of the authors (MA) gratefully acknowledges support during the revision stage of this manuscript by Sandia National Laboratories. Sandia National Laboratories is a multi-program laboratory managed and operated by Sandia Corporation, a wholly owned subsidiary of Lockheed Martin Corporation, for the U. S. Department of Energy's National Nuclear Security Administration under contract DE-AC04-94AL85000.

References

[1] H. Lei, B. Caswell, and G. E. Karniadakis, *Physical Review E*, 81(4):026704:1-10 (2010).
[2] Tiwari, A., and Abraham, J. *Microfluid. Nanofluid*. 4(3), 227 (2008).
[3] Moseler, M. and Landman, U., *Science* 289: 1165 (2000).
[4] Pagonabarraga, I., and Frenkel, D., *J. of Chemical Physics*, 115:11:5015-5026 (2001).
[5] Warren, P. B., *Physical Review E*, 68:066702, 2003.
[6] Trofimov, S. Y., Nies, E. L. F., and Michels, M. A. J., *J. of Chemical Physics*, 123(14):144102 (2005).
[7] Arienti, M., Pan, W., Li, X, and Karniadakis, G., *J. of Chemical Physics*, 134, 204114 (2011).
[8] Plimpton, S. J., *J. of Computational Physics*, 117(1):1-19 (1995).
[9] Groot, R. D., and Warren, P. B., *J.l of Chemical Physics*, 107:11:4423-4435 (1997).
[10] Visser, D. C., Hoefsloot, H. C. J., and Iedema, P. D., *J. of Computational Physics,* 214: 491-504 (2006).
[11] Backer, J.A., Lowe, C.P., Hoefsloot, H.C.J., Iedema, P.D., *J. of Chemical Physics* 122 (15): 154503 (2005).
[12] Bugel, M., Galliero, G., and Caltagirone J.-P., *Microfluid. Nanofluid*. 10(3): 637-647 (2010).
[13] Eggers, J., *Phys. Review Letters*, 71:3458-3460 (1993).
[14] Eggers, J., *Phys. Review Letters*, 89:084502 (2002).
[15] Arienti, M., ILASS Americas, 23rd Annual Conference, Ventura, CA, May 2011.